Comparative analysis of SAOCOM and Sentinel-1 data for surface soil moisture retrieval using a change detection method in a semiarid region (Douro River's basin, Spain)

Benedetta Brunelli [a,b,*], Francesco Mancini [b]

[a] *Department of Environmental Engineering, University La Sapienza, Str. Eudossiana, 18, Roma, 00184, Italy*
[b] *Department of Engineering E.Ferrari, University of Modena and Reggio Emilia, Str. P. Vivarelli, 10, Modena, 41125, Italy*

ARTICLE INFO

ABSTRACT

The growing interest in low-frequency SAR for soil parameter retrieval has led to the development of new active L-band satellites, that will provide novel surface soil moisture products and retrieval possibilities; however, due to data unavailability so far, limited applications have investigated the use of change detection models using L-band satellite SAR data. Since July 2020, high revisit time, high-resolution acquisitions by the Satélite Argentino de Observación COn Microondas (SAOCOM) Argentinian-Italian constellation have become accessible over Europe. Therefore, this research presents an investigation of the potential of multi-temporal L-band SAOCOM-1 for monitoring soil moisture variations underneath low and sparse agricultural vegetation. Moreover, it proposes a procedure for the mitigation of roughness contribution, by exploiting the entropy parameter derived from the dual-polarimetric decomposition. L-band sensitivity to soil moisture has been jointly evaluated in respect of Sentinel-1 C-band data by (1) comparing the temporal profiles of the backscattering coefficient, γ^0, at VV and VH polarization, with the support of decomposition parameters (entropy and $\bar{\alpha}$), NDVI and precipitation data; (2) regression analysis with in situ soil moisture measurements, obtained by the REMEDHUS network in the Douro River basin (Spain); 3) evaluating the soil moisture retrievals obtained at C- and L- band using a change detection method. Finally, the effectiveness of the roughness normalization procedure for SAOCOM data has been validated using in situ data. L-band co-polarized γ^0 has proved to be the best configuration for soil moisture inversion, being relatively insensitive to vegetation, as demonstrated by decomposition results and trend interpretation. Overall, regressions detected an R^2 22% higher at L-band than C-band, with values up to 0.74 for VV ($\bar{R}^2$=0.32) and up to 0.47 for the VH band ($\bar{R}^2$=0.14). Co-polarized data obtained R^2 on average 62.1% and 74.7% higher for SAOCOM and Sentinel-1. The retrieval models show an ubRMSD of 7.1% for SAOCOM data and 8.3% for Sentinel-1. The application of the proposed roughness normalization procedure to SAOCOM led to an ubRMSD of 6.7% improving the retrieved soil moisture trend by 7.9%. This exploratory analysis demonstrated SAOCOM data potential for soil moisture mapping and would serve as a foundation for more advanced retrieval procedures.

1. Introduction

Soil Moisture (SM) is a fundamental land-surface boundary condition, which plays a key role in numerous processes involved in the climate system, in the water, energy, and carbon cycle. The concern about SM decrease in southern Europe, and its associated environmental and socio-economic impacts, makes large temporal and spatial scale monitoring of SM particularly relevant for an enlightened water and soil resources management (Li et al., 2022).

In the past 50 years, microwave RS using Synthetic Aperture Radar (SAR) instrumentation has proved to be an exceedingly powerful means for measuring Superficial SM (SSM) dynamics over regional and global scales. The exploitation of the microwave region allows for overcoming some of the main limitations associated with optical/infrared bands, such as reduced soil penetration, cloud cover disturbance, and natural energy sources exigency, ensuring a usable acquisition in each overpass and thus a high temporal frequency. In addition, SAR technology makes it possible to obtain high geometric resolutions both in the azimuthal and in the range direction. The models developed to address the problem of soil moisture recovery from SAR data can be traced back to two main approaches: (1) instantaneous algorithms, generally grouped

---

into theoretical, empirical and semi-empirical (Hajnsek et al., 2003; Fung et al., 1992; Oh et al., 1992); (2) and multi-temporal or change-detection (CD) algorithms (Wagner et al., 1999b; Bauer-Marschallinger et al., 2018). Each technique presents different challenges and limitations related to the accuracy and resolution of the final product; the exportability and general enforceability of the models; the calibration and validation procedures. Calibration and validation-related issues regard mainly the comparison between different spatial and temporal resolutions datasets, in-situ data availability and reliability, and the choice of the metric used to quantify the accuracy of the estimates - the Quality Assurance Service for Satellite Soil Moisture Data (QA4SM) is an example of a standardized validation procedure (Preimesberger et al., 2022). On the other side, the accuracy and exportability of the method depend greatly on how the impacts of surface geometry and biophysical properties of the soil are taken into account. Nowadays, SSM operative mapping is achieved using (1) C-band SAR images, taking advantage of the continuous supply of Sentinel-1 and ASCAT radiometer data (Hamze et al., 2021), and (2) L-band passive sensors, such as AMSR-2, SMOS, and SMAP radiometers (Petropoulos et al., 2015). L-band SAR was also proved to be highly sensitive to SSM, using satellites (Gururaj et al., 2021), and mainly airborne and UAVSAR datasets (Bhogapurapu et al., 2022), with which different frequencies and multi-frequency approaches (Balenzano et al., 2010; Abdikan et al., 2023) were tested. Indeed, longer wavelengths, due to their penetration capabilities through the canopy, are more suitable for soil parameter retrieval in vegetated areas, whereas C and higher frequencies wavelengths carry more information on vegetation dynamics. Magagi et al. (2022) have found that differently polarized Normalized Radar Cross Sections (NRCSs) at the L-band are significantly more correlated to SSM over vegetated areas than at C-band. Other studies, such as El Hajj et al. (2019), found that the L-band provides less accurate retrievals than the C-band, due to the underestimation of SSM in the case of slightly rough surfaces. The impact of roughness on the inversion models can be mitigated using single or multi-frequency polarimetric approaches (Hajnsek et al., 2003; Hamze et al., 2021). Whereas the use of polarimetric parameters, such as entropy and $\bar{\alpha}$, (Cloude and Pottier, 1996) to "directly" estimate soil moisture has led to inconclusive results (Baghdadi et al., 2012), their potential to disentangle the scattering mechanisms has been proved for quad-polarized data (Koch et al., 2012) and, taking into account for their smaller range of variability in case of lack of co-polarization channels (Ji and Wu, 2015), also for dual-pol data (Harfenmeister et al., 2021) (Section 2.2.1). The magnitude of roughness and vegetation contributions, as well as penetration depth through the soil, are frequency-dependent; therefore, upcoming L-band SAR missions, such as ALOS-4 (2023), NISAR (2024), Tandem-L (2024), and Rose-L (2028), will provide SSM retrievals carrying different pieces of information with respect to the currently available products. However, due to the lack of feasible L-band data, limited applications, e.g. ESA campaigns such as the AgriSAR (2006), for which Balenzano et al. (2010) applied a short-term change detection approach to airborne L-band data, have investigated CD models using L-band SAR data. In this context, SAOCOM data, which have been available since July 2022 with a temporal frequency of 8 days, constitute a great opportunity to explore different bands' strengths and weaknesses for SSM retrievals, as well as varied responses to soil and vegetation properties.

This work aims indeed to compare the potential of L-band SAOCOM and C-band Sentinel-1 data to track soil moisture variations underneath sparse crops using γ^0s, i.e. the backscattering coefficient normalized by the cosine of the incidence angle, through trend analysis, regression techniques and a well-known CD model implemented over both datasets. Moreover, it is proposed a novel procedure for the mitigation of the roughness contribution at L-band, based on the dual-polarimetric decomposition entropy parameter. The methodologies were tested in a central semiarid sector of the Douro basin (Spain), where in-situ SSM measurements provided by the Red de Estaciones de Medición de la Humedad del Suelo (REMHEDUS) network were used for calibration

and validation purposes. This exploratory analysis is the first example of the application of a CD model with SAOCOM dataset, and therefore it aims to serve as a foundation for its use in more comprehensive or multi-frequency approaches.

2. Materials and methods

2.1. Materials

In this section, the agricultural study area in Spain is presented; subsequently, in-situ and satellite data main characteristics and scope are described.

2.1.1. Study area and in-situ data

The study area is an agricultural region of approximately 1300 km^2 located in the central part of the river Douro basin (Spain) (Fig. 1a–b). It is characterized by a semiarid Mediterranean climate, an elevation between around 600 m and 900 m above sea level, and a mean slope of 2% (Fig. 1c). Mainly calcisoil and fluviosoil are found in the area (Fig. 1d). According to the 2018 Corine Land Cover (CLC) dataset, agricultural areas, which cover 87% of the region, are mainly intended for rainfed cereals, irrigated crops, and vineyards. Non-cultivated areas, 13% of the region, are covered by forests and shrubs (Fig. 1e). In the area, sensors belonging to the REMEDHUS network have been installed since 2005. It is constituted of 24 stations (18 currently active) spread across the region and it monitors SSM and soil temperature. SSM measurements are provided hourly by each station in the top 5 cm of the soil with Stevens Hydra Probes, which has an accuracy of 0.003 m^3/m^3 (Pablos et al., 2016). REMEDHUS data are nested in the International Soil Moisture Network (ISMN) (Dorigo et al., 2021) which standardizes the datasets in terms of unit (m^3/m^3) and sampling rates (hourly), and applies a quality control through an automated flagging methodology. In situ data for 4 stations showed a variability range of SSM below 1% (ElCoto, ElTomillar) and 2% (LasBrozas and LasVictorias), and very low maximum SSM content (ElCoto: 4%, ElTomillar: 6%, LasBrozas: 15%, LasVictorias: 16%), with values exceeding 10% only a few days during the year. Usually, the studies carried out on the L-band sensitivity focus on a condition of SSM greater than 10% (Kim and Van Zyl, 2009). Liu et al. (2016), demonstrated that, at L-band, volume effects take place when SSM < 7%, and that the sensitivity of the backscattering coefficient to SSM at VV polarization is of 1 dB/1%. Since we use a linear model to compare C- and L-band estimates, and the description of volumetric scattering behavior is not addressed in the present work, the 4 stations mentioned above were discarded from the analysis (Fig. 1b.).

2.1.2. Satellite data

In the current section, the satellite datasets, acquired in 2022 and consisting of 81 SAR images (21 SAOCOM and 60 Sentinel-1), and 60 Sentinel-2 images, are described (Fig. 2).

SAOCOM Argentine-Italian SAOCOM-1 (Satélite Argentino de Obserevacion Con Microondas) Constellation is the polarimetric L-Band SAR mission operated by the Comisión Nacional de Actividades Espaciales (CONAE) and composed of two twin spacecraft, SAOCOM-1 A, and SAOCOM-1B, launched respectively in October 2018 and August 2020 (Recchia et al., 2022). The goal of the mission is to obtain high revisit frequency, radiometric and geometric accuracy SAR data to support agricultural, hydrological, and interferometric applications. The full constellation has a revisit time of 8 days, thanks to the 180° nominal separation between the two satellites, which follow sun-synchronous, semi-polar orbits at a mean altitude of 620 km. These orbits are shared with the X-band COnstellation of small Satellites for Mediterranean basin Observation (COSMO) Skymed, forming the Italian-Argentinian satellite system for Disaster Management and economic development (SIASGE), the double-band joint mission between the Agenzia Spaziale
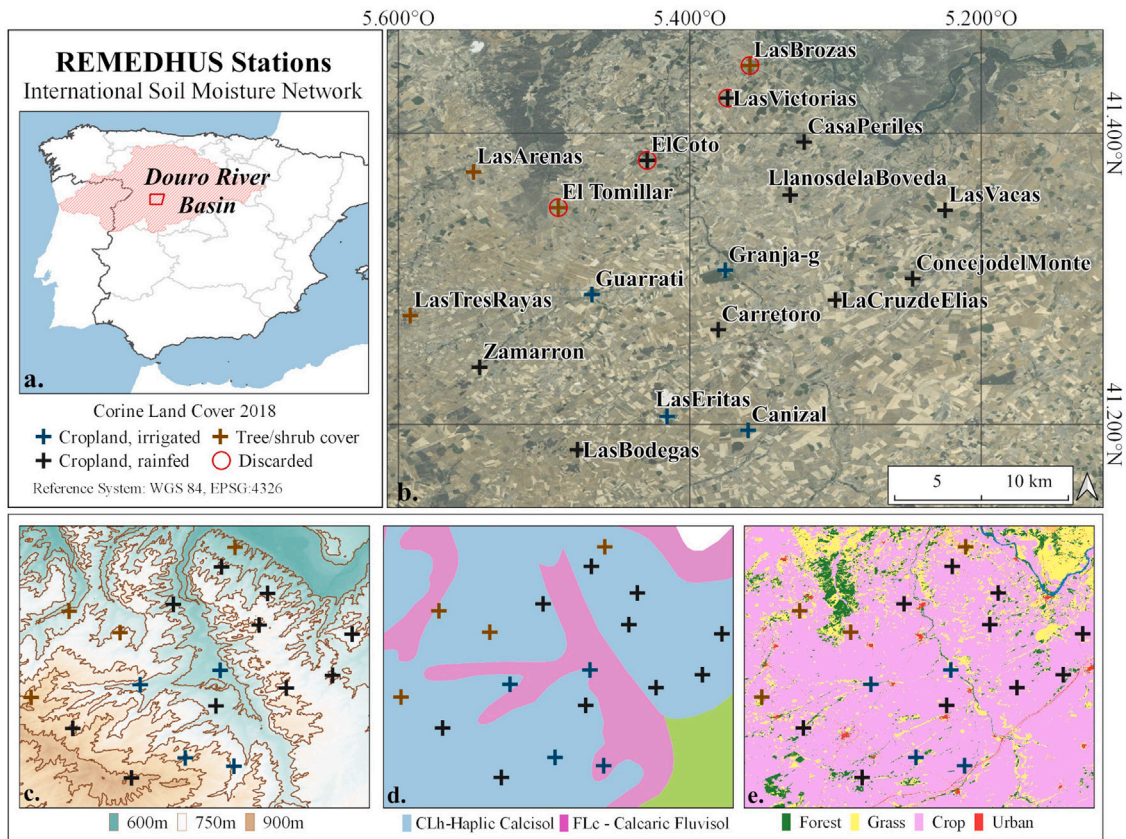
Fig. 1. Study area and location of the REMEDHUS network stations. a. shows the Douro River basin and the framework. In b. REMEDHUS stations, distinguished by Land Use Land Cover (LULC) derived from CLC map (2018) are located over the Esri World Imagery basemap (red circles indicate a station discarded from the SSM retrieval). In c. the 30 m Digital Elevation Model (DEM) and contour lines show the topography of the study area. In d. the FAO90 soil types from the European soil database are reported. e. shows the main land use with ESA World Cover 2021. (For interpretation of the references to color in this figure legend, the reader is referred to the web version of this article.)
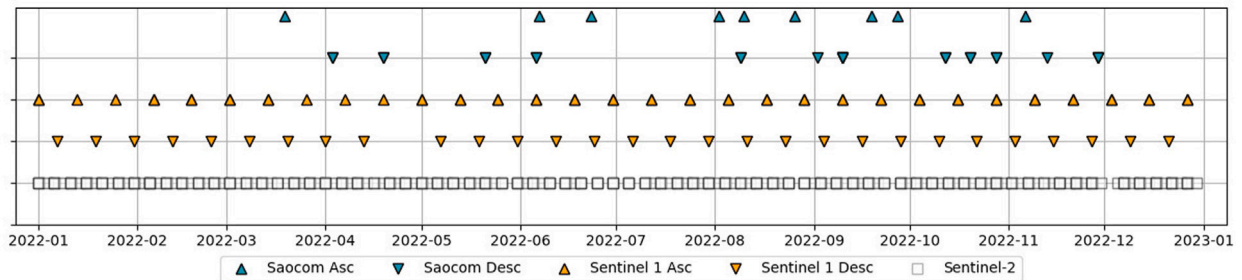

Fig. 2. Dates and orbit direction of satellite data acquisitions during 2022.

Italiana (ASI) and CONAE (Azcueta et al., 2021). SAOCOM SAR instruments work at a frequency of 1275 MHz and a maximum bandwidth of 50 MHz; the Noise Equivalent Sigma Zero (NESZ) is assessed at −34 dB for full or quad polarimetric (QP) mode and −28 dB for dual/single (DP/SP) polarization. SAOCOM was conceived as a multi-modes and multi-swath mission, which is capable of focusing targets at different terrain locations using ranges of incidence angles. This system is also designed to maximize the coverage and allow compatibility with the COSMO mission acquisitions. Combining the two polarization, the three acquisition modes, and the beam positions along the range direction, 25 acquisition modalities can be obtained. Stripmap (SP) at dual-polarization is the default acquisition mode, with incidence angles comprised between 21° and 50°, a swath width of 30 km to 67 km, a resolution of 10 m × 5 m (range × azimuth) and 9 beams. Overall, SAOCOM design allows for having an absolute radiometric accuracy below the requirement of 1 dB for both Stripmap QP (0.1 dB) and Stripmap SP/DP (0.3 dB), as shown by the Impulse Response

Function (IRF) validation (Recchia et al., 2022). Regarding geolocation, CONAE provides two types of orbit ephemeris, by whose precision the geolocation accuracy of the data depends. The faster ephemerids are used in the absolute georeferencing process realized with onboard GPS, the so-called On-Line Very Fast (OLVF) orbit determination, and ensure a geolocation accuracy of better than 90 m on the ground; whereas the precise ones, i.e. Off-Line Fast (OLF) orbit determination, are used after two days and result in an accuracy of 55 m, below the requirements of 70 m (Recchia et al., 2022). Accurate geocoding is crucial since SAOCOM has an unstable orbital tube, which causes wide variability of the perpendicular spatial baseline (Seppi et al., 2022) and therefore may affect coherence and InSAR processing. SAOCOM products acquired in the Zone of Exclusivity, i.e. the geographic zone in which ASI has utilization rights, which correspond to the European territory, are available since July 2022 through the ASI portal. For the area regarded in this work, only Stripmap DP (VV/VH), with OLF orbit determination, time series images were available for download.

The preprocessing level is Single Look Complex (SLC), i.e. slant-range images, not multi-looked or geometrically corrected and represented by complex values. Unlike S1 SLC, these data are radiometrically calibrated. In particular, 9 ascending orbit and 12 descending orbit images acquired in 2022 are used (Fig. 2). The temporal baseline is variable from 1 to 40 days, considering both orbits. These images were acquired at the S4 beam position, therefore they have a minimum swath width of 65.7 km and an incidence angle of 33.7° to 38.3° (Rosenqvist et al., 2014).

The preprocessing applied for SAOCOM SLC using the Sentinel Application Toolbox (SNAP) aimed to obtain γ^0_{VV} and γ^0_{VH} values at the resolution of 10 m. The terrain flattening operator was applied to mitigate the effect of the incidence angle and topography; this method, proposed by Small (2011), enables the combined use of multi-track and multi-sensor backscatter time series. Arias et al. (2022a) demonstrated that it was able to remove the impact of incidence angle at VH and reduce it significantly at VV, with backscattering values differences amongst simultaneous different orbits acquisition below 0.8 dB. Tested by Dostalova et al. (2022), it improved the classification's accuracy up to 20% in regions with strong topography. The Refined Lee filter was used to attenuate the speckle; the Range-Doppler terrain correction geocoded the images using the Copernicus 30 m DEM and WGS84 Reference System. Finally, linear to dB conversion was applied. Polarimetric decomposition has been obtained by including in the previous pre-processing workflow the calculation of the dual-polarimetric coherency matrix and the dual-polarimetric entropy-$\bar{\alpha}$ decomposition.

Sentinel-1 Sentinel-1 mission comprises a constellation of two polar-orbiting satellites, both carrying a C-band SAR dual-polarized instrument with a frequency of 5.405 GHz and a revisit period of 12 days. For this study, S1 A and S1B data at interferometric wide swath (IW) mode and Level-1 SLC of processing were used. IW acquires data with a 250 km swath (almost 4 times larger than SAOCOM's) at 5 m by 20 m spatial resolution and an incidence angle θ_i which ranges between 29° and 46°. Ascending and descending images have relative orbit numbers of, respectively, 62 and 29 (Fig. 2). The following pre-processing was applied in SNAP at SLC images to obtain γ^0_{VV} and γ^0_{VH} at the resolution of 10 m: orbit file for precision geolocation, S1-TOPS split, radiometric noise removal, radiometric calibration, S1-TOPS deburst, S1-TOPS merge, terrain flattening, Refined Lee Filter, and Range-Doppler terrain correction using the Copernicus 30 m DEM. As for SAOCOM data, the polarimetric preprocessing implemented the additional dual polarimetric matrices calculation and dual-polarimetric entropy-$\bar{\alpha}$ decomposition.

Sentinel-2 Sentinel-2 is a multi-spectral imaging mission with two polar-orbiting satellites carrying a Multispectral Instrument (MSI) that acquires passively in 13 spectral bands. In this work, 140 Sentinel-2 Level 2 A Harmonized images, available in the Google Earth Engine (GEE) cloud-computing platform, were used (Fig. 2). After applying a cloud mask using the Sentinel-2 Quality Assessment (QA) band, the NDVI index was calculated at each station and the results were subsequently exported from GEE.

2.2. Methods

The dual polarimetric decomposition method, for the calculation of entropy and $\bar{\alpha}$ parameters, and the soil moisture change detection model are recalled in this section. Finally, it is proposed a novel procedure based on the entropy parameter for mitigating the contribution of roughness changes on the backscatter.

2.2.1. Dual-polarimetric decomposition

The entropy-$\bar{\alpha}$ polarimetric decomposition, originally designed for fully-polarimetric data, allows the differentiation of the scattering mechanisms occurring within each resolution cell (Cloude and Pottier, 1996; Ji and Wu, 2015). The scattering matrix [S], used to represent the polarimetric information measured by the radar in deterministic targets, can be vectorized into the 2-D (for dual-polarimetric data) unitary Pauli vector $\bar{k}$, as in Eqs. (1) and (2):

$$\bar{k} = \frac{1}{\sqrt{2}} [S_{VV} \, 2S_{VH}]^T \tag{1}$$

$\bar{k}$ can be described by 1 angle, α, and 2 phases, γ and δ_i:

$$\vec{k} = \begin{bmatrix} \cos(\alpha_i)exp(i\gamma_i) \\ \sin(\alpha_i)exp(i\delta_i) \end{bmatrix} \tag{2}$$

The dual-polarimetric coherency matrix $\langle C \rangle$, in Eq. (3), used to describe incoherent scattering transformations, is calculated for both SAOCOM and Sentinel-1 images:

$$\langle C \rangle = \langle k \cdot k^T \rangle_n = \sum_{i=1}^{n} k_i \cdot k_i^T \tag{3}$$

where k_i represents the scattering vector of the ith pixel, as defined in Eq. (1), and n represents the number (9 in this work) of pixels averaged (Alonso-Gonzalez and Papathanassiou, 2022). Throughout the eigenvectors and eigenvalues decomposition two orthogonal scattering matrices are obtained by Eq. (4):

$$\langle C \rangle = [T_1] + [T_2] = \lambda_1 \cdot (\vec{v}_1 \cdot \vec{v}_1 \ast) + \lambda_2 \cdot (\vec{v}_2 \cdot \vec{v}_2 \ast) \tag{4}$$

where each eigenvector $\vec{v}_i$ corresponds to a scattering mechanism, while the related eigenvalue λ_i expresses the importance of the corresponding scattering mechanism with respect to the Total Power ($TP = \lambda_1 + \lambda_2$). Entropy, H, which expresses the degree of randomness of the scattering mechanism, is retrieved from Eq. (5):

$$H = \sum_{i=1}^{2} p_i \cdot log_2(p_i)$$
$$p_i = \frac{\lambda_i}{\sum_{i=1}^{2} \lambda_i} \tag{5}$$

where p_i expresses the relative importance of the corresponding λ_i on the TP. The $\bar{\alpha}$ angle, in Eq. (6), describes the averaged scattering mechanisms.

$$\bar{\alpha} = \sum_{i=1}^{2} p_1 \cdot \alpha_i \tag{6}$$

In the case of dual-polarized data, $\bar{\alpha}$ is the mean between the α derived from the dominant $\vec{v}_1$ and the perpendicular non-dominant one. For fully polarized data, $\bar{\alpha} \rightarrow 0$ is associated with surface scattering; $\bar{\alpha} \rightarrow 45°$ indicates dipole, and $\bar{\alpha} \rightarrow 90°$ indicates dihedral scattering. Whereas, for dual VV-VH polarized data, the lack of a co-polarized channel causes the diffusion and overlap of the scattering mechanisms in the entropy-$\bar{\alpha}$ plan plot, with $\bar{\alpha}$ values constrained below 45°. The thresholds for their extraction depend on the polarimetric channels considered and should be empirically determined (Ji and Wu, 2015). However, relative value differences between land covers or frequencies can be used to highlight different scattering behaviors and classify the target (Banque et al., 2015; Brunelli et al., 2023).

2.2.2. Soil moisture change-detection model

The soil moisture change detection method, initially proposed by Wagner et al. (1999a) for the ERS scatterometer, was adapted to Sentinel-1 data (Bauer-Marschallinger et al., 2018), and it is currently implemented for the production of the SSM at 1 km resolution within the Copernicus Global Land Service. It assumes time-invariant roughness and vegetation conditions while neglecting multiple scattering mechanisms in crop canopies. It is summarized in Eqs. (7) and (8):

$$SSM_r(t) = \frac{\sigma^0_{VV} - \sigma^0_{VVmin}}{\sigma^0_{VVmax} - \sigma^0_{VVmin}} \quad [\%] \tag{7}$$

where $SSM_r(t)$ is the relative soil moisture content at time t, linearly scaled between dry, σ^0_{VVmin}, and wet, σ^0_{VVmax}, reference values. These

correspond respectively to the minimum and maximum values of the backscattering coefficient through the time series for each sample. σ^0_{VVmin} is subtracted from the current radar image to implicitly account for the terrain geometrical property. To mitigate the dependence of the radar backscatter on the incidence angle, σ^0 is typically normalized to a mean θ_i value using a slope approach (Widhalm et al., 2018). The effectiveness of this method is related to the number of scenes considered and the incidence angle range, which both differ in SAOCOM and Sentinel-1 datasets. Therefore, in order to apply a standardized procedure to both datasets in SNAP, the present work relies instead on the use of the terrain flattened γ^0 coefficient, which obtains comparable mitigation of the incidence angle effect, as well as a topography correction (Section 2.1.2). $SSM_r(t)$, in Eq. (8), is converted to volumetric soil moisture, $SSM_v(t)$, using the saturation, sat, and wilting point, $wilt$, values.

$$SSM_v(t) = SSM_r(t) \cdot (sat - wilt) + sat \quad [\text{m}^3/\text{m}^3] \tag{8}$$

where sat and $wilt$ are volumetric soil moisture measurements empirically obtained from in-situ data. Finally, the performance metrics used are reported in Eqs. (9)–(12).

$$RMSD = \sqrt{\frac{\sum_{i=1}^{N}(y_i - \tilde{y}_i)^2}{N}} \quad [\text{m}^3/\text{m}^3] \tag{9}$$

$$bias = \sum_{i=1}^{N} |y_i - \tilde{y}_i| \quad [\text{m}^3/\text{m}^3] \tag{10}$$

$$ubRMSD = RMSD - bias \quad [\text{m}^3/\text{m}^3] \tag{11}$$

$$R^2 = 1 - \frac{\sum_{i=1}^{n}(y_i - \tilde{y}_i)^2}{\sum_{i=1}^{n}(y_i - \bar{y}_i)^2} \tag{12}$$

where $y(i)$ is the estimated SSM value, and $\tilde{y}(i)$ is the measured one. The Root-mean-square deviation ($RMSD$) expresses the retrieval accuracy with a quadratic penalty for outliers, and the $ubRMSD$ excludes stationary biases. Indeed, SSM retrievals biased in the absolute magnitude of soil moisture content are still useful if they reproduce the actual trends measured in the ground. Whereas $RMSD$ is expressed in m³/m³, R^2 is a dimensionless metric used to capture the time series correlation, regardless of biases in mean and variance (Entekhabi et al., 2010).

2.2.3. Roughness normalization

At coarse resolution, the model's premise of constant roughness over time is supported by the assumption that roughness-driven signals induced by individual features are minimized as they sum up incoherently within each sample (Bauer-Marschallinger et al., 2018). When considering the radar intensity at the field scale, roughness affects the backscatter value by reflecting soil and vegetation geometrical structure, which varies due to tillage practices, modification in crop orientation, size, etc. Therefore, a procedure to stabilize the roughness-induced variations is proposed. It relies on the entropy parameter extracted through the dual-polarimetric decomposition (Section 2.2.1). In ideally smooth surfaces, non-depolarizing surface scattering processes would be characterized by zero entropy, meaning that the Total Power is completely described by a single (surface) retrieval matrix i.e. $\lambda_1 = 1; \lambda_2 = 0$. Natural rough surfaces depolarize the signal; as the roughness increases, the contribution of the secondary perpendicular scattering mechanism increases, as well as the entropy value. Therefore, entropy is here used as a proxy for roughness changes; however, because entropy is also sensitive to canopy structure, the application of the proposed roughness normalization relies on two assumptions:

1. entropy is not affected by the dielectric constant, which is demonstrated by Hajnsek et al. (2003), where the polarimetric parameters are used to disentangle soil moisture and roughness contribution;

2. surface scattering is dominant in the fields considered for the retrieval, and thus it is described by the first eigenvector. This is supported by the fact that NDVI values fall below 0.3; moreover, the procedure is applied only to L-band SAOCOM data, which can penetrate low-density vegetation, and are characterized by mean $\bar{\alpha} < 15°$ and H < 0.4 which, according to Ji and Wu (2015), correspond to Bragg surface in the VV/VH case. Studies that decompose fully polarimetric L-band data show that surface scattering dominated for alfalfa, winter wheat, and summer crops over most of the year (Li et al., 2019).

As surface roughness increases both the backscattering and the entropy value increases; this relationship is here simplified using a linear model. Fig. 3 shows the scatterplot of entropy and γ^0_{VV} on the entire dataset, excluding forested and urban areas. The slope of the linear regression line, β, is then used to normalize the images for roughness, as in Eq. (13):

$$\gamma^0(0.3,t) = \gamma^0(H,t) - \beta \cdot (H - 0.3) \quad [\text{dB}] \tag{13}$$

where $\gamma^0(0.3,t)$ is the backscatter coefficient normalized for the entropy value of 0.3, which is the average for each in-situ station (Section 3).
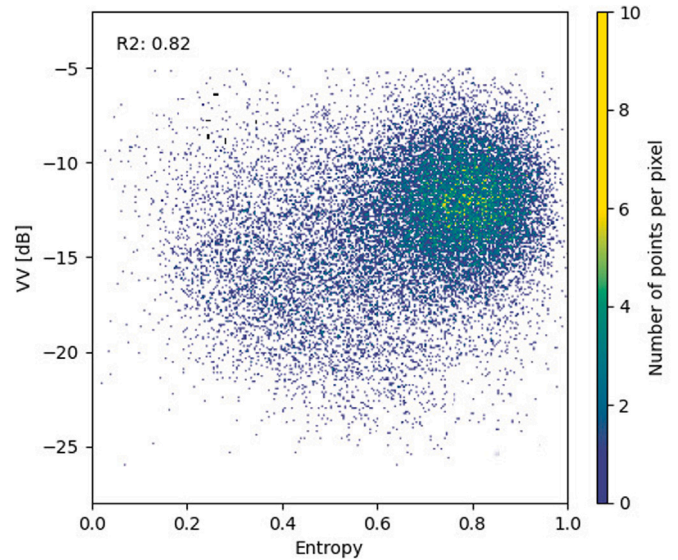

Fig. 3. Correlation between entropy and γ^0_{VV} calculated from the entire SAOCOM dataset over the area shown in Fig. 1b. Forested and urban areas are masked using Corine LULC classes (2018).

3. Results

In this section, γ^0 temporal profiles and regression analysis are shown. As the single-pixel amplitude values can oscillate due to the affection of residual noise, this analysis refers to the mean γ^0 value among a rhomboidal area of 9 samples (90 m²) centered in each station's pixel (Graldi and Vitti, 2022). The averaged parameters, at each acquisition, are used for time series, correlation and prediction. Finally, the application of the roughness normalization procedure and the change detection models are described.

3.1. Temporal series of γ^0

Radar backscattering trends are representative of the biogeophysical and geometrical properties of the soils; in addition, the superimposed effect of the vegetation layer causes seasonal variability over agricultural areas. Below, the temporal series of γ^0_{VV} and γ^0_{VH} for SAOCOM and Sentinel-1 data are compared with the support of precipitation data, linked to soil and vegetation content, and NDVI variation, used as a proxy for vegetation greenness and density. In Fig. 4 these temporal series are reported for 14 stations of the network.
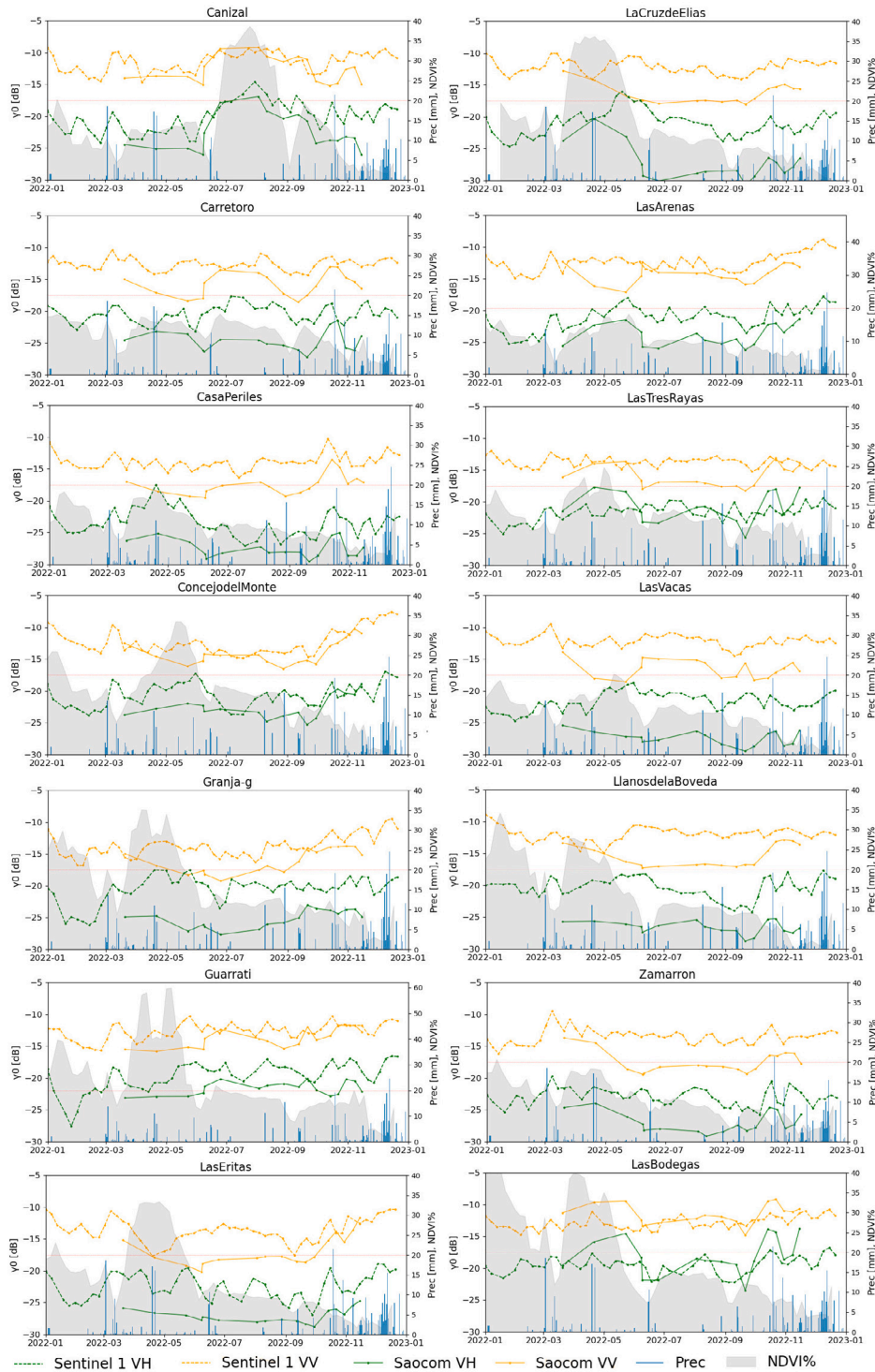
Fig. 4. Backscatter variations during the year as a function of different polarization channels and frequencies. γ^0 [dB] is the mean value calculated over 9 samples centered around each station. Continuous lines indicate SAOCOM data and dashed lines indicate Sentinel-1. Co-pol data are colored in orange and cross-pol in green. (For interpretation of the references to color in this figure legend, the reader is referred to the web version of this article.)

Among all stations, L-band data values range between −31.1 dB and −15.7 dB for cross-polarized signals and −20.7 dB to −8.6 dB for the co-polarized ones; whereas C-band data range between −30.4 dB and −14.2 dB for VH and between −20.2 dB and −0.1 dB for VV. The difference between SAOCOM VV and VH is comprised between 5.0 dB to 12.8 dB, and has a mean value of 9.2 dB; whereas the difference between Sentinel-1 VV and VH goes from 5.7 dB to 9.1 dB, with a mean value of 7.5 dB. The lower Relative Standard Deviation (RSD) is

detected for L-band and VH polarization (RSD = 9.3%), then for C-band VH (RSD: 10.2%), C-band VV (RSD: 13.8%) and L-band VV (14.6%). Generally, vegetation growth causes the backscattering coefficient to increase: on average, an NDVI increase of 10% corresponds to a γ^0 increment of 0.4 dB for VV at the L-band and of 0.6 dB at the C-band; in the VH channel it increases of 1.1 dB for the L-band and of 1.3 dB at C-band. On the other side, precipitations show a more moderate impact: after 56.5 mm of rain fell in the second half of
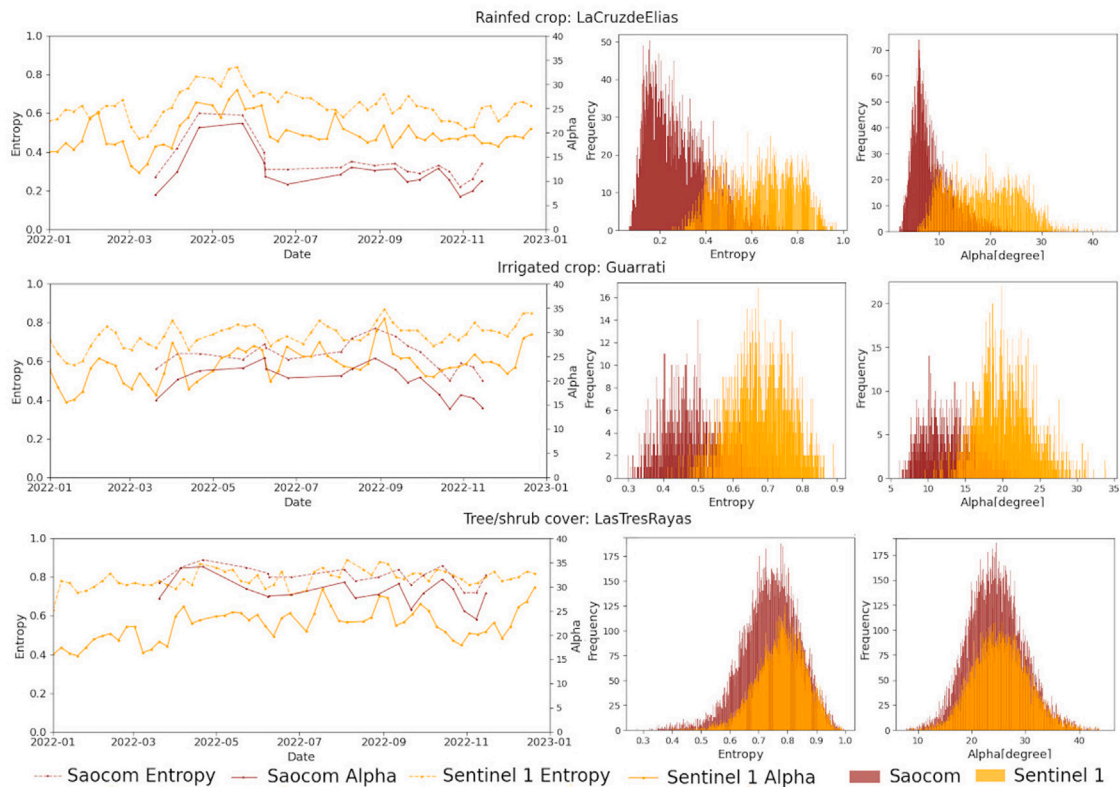
Fig. 5. On the left, entropy and $\bar{\alpha}$ temporal variations of SAOCOM and S1 images are presented for three ISMN stations. On the right, frequency histograms represent the variations of these parameters in the fields around the stations for an L-band and a C-band images. Each station represents a different land cover class: rainfed (LaCruzDeElias), irrigated (Guarrati) crops, and three or shrub cover (LasTresRayas).

October, γ^0 has increased (from 22nd October to 30th of October) by 2.8 dB for VV at the L-band and of 6.9 dB at the C-band; in the VH channel, it increases of 2.8 dB for the L-band and remains stable at C-band. A comparison of the backscattering mechanisms is carried out by studying the polarimetric transformation through the entropy and $\bar{\alpha}$ parameters and as a function of different LULCs. Fig. 5 compares the pixel frequency histograms calculated from the whole scene for three major land cover classes derived from CLC 2018. In general, $\bar{\alpha}$ angle values for crop fields are comprised between 9° and 22° for the L-band (an exception is represented by LaCruzdeElias), and between 16° and 29° for the C-band. In tree-covered fields, they fall between 13° to 21° for L-band and 19° to 21° for C-band. For Sentinel-1 data entropy values are between 0.6 and 0.7 for crop and 7.8 for tree-covered stations. For SAOCOM these are respectively between 0.2 and 0.6 and between 0.4 and 0.6. Fig. 6 shows a visual comparison between H and $\bar{\alpha}$ parameters calculated from L- and C-band.

3.2. Correlation of γ^0s with SSM

Over the 14 validation sites, a positive correlation is detected in 10 and 4 stations respectively for L- and C-band; regression values show better performance for SAOCOM data (mean R^2 VV: 0.302, max 0.745, mean R^2 VH: 0.130, max: 0.4754) with respect to Sentinel-1, which are overall not correlated (max R^2 VV: 0.249, max R^2 VH: 0.102) (Fig. 7). The VV band for both satellites performs better than VH, obtaining R^2 on average 62.1% and 74.7% higher for SAOCOM and Sentinel-1. Mean R^2 values for L-band at the VV polarization are similar for irrigated crop (0.312) and rainfed crop (0.318); whereas is lower for tree/shrub stations (0.185). At VH polarization irrigated crops show a better correlation (0.185) than rainfed (0.185) and tree/shrub (0.045). In general, for tree-covered fields R^2 declines by 41% at VV and by 75% at VH with respect to crop. At C-band, VH correlation values are below 0.11, while for VV polarization, the best result is obtained in rainfed crops with a mean R^2 0.145.

3.3. Surface soil moisture retrieval

The long-term change detection model was applied to co-polarized data at L- and C-band, which showed a correlation with soil moisture measurements. The model was calibrated using empirical values (Section 2.2.2); after flag application the mean saturation value is 0.031 m^3/m^3 and the wilting point value is 0.288 m^3/m^3. The normalization procedure was applied to SAOCOM data before the application of the CD model. Subsequently, model performances at C-band, L-band not-normalized, $\gamma^0(H,t)$, and L-band normalized, $\gamma^0(0.3,t)$, were evaluated. The scatterplots between the measured and retrieved soil moisture are shown in Fig. 8. $RMSD$ and $ubRMSD$ are respectively 0.084 m^3/m^3 and 0.071 m^3/m^3 for L-band $\gamma^0(H,t)$ data and 0.099 m^3/m^3 and 0.083 m^3/m^3 for C-band data. $\gamma^0(0.3,t)$ obtain values of 0.088 m^3/m^3 and 0.067 m^3/m^3 and the higher R^2, 0.562, compared to L-band not normalized data (0.483), and C-band data (0.330). Fig. 9 compares SSM retrievals obtained with different frequency datasets.

4. Discussion

Some observations arising from the results are discussed in the current section.

4.1. Co- and cross-polarization comparison

Soil and vegetation properties affect amplitude magnitude over time depending on the system's polarizations. Overall co-polarized signals are stronger than the cross-polarized ones, regardless of the frequency. The RSD calculation (Section 3.1) has shown that at L-band VH polarization trends are overall stabler than VV, whereas at C-band VV is more stable than VH. Indeed, for C-band, the signal's depolarization is significantly influenced by crop phenological phase (Balenzano et al.,
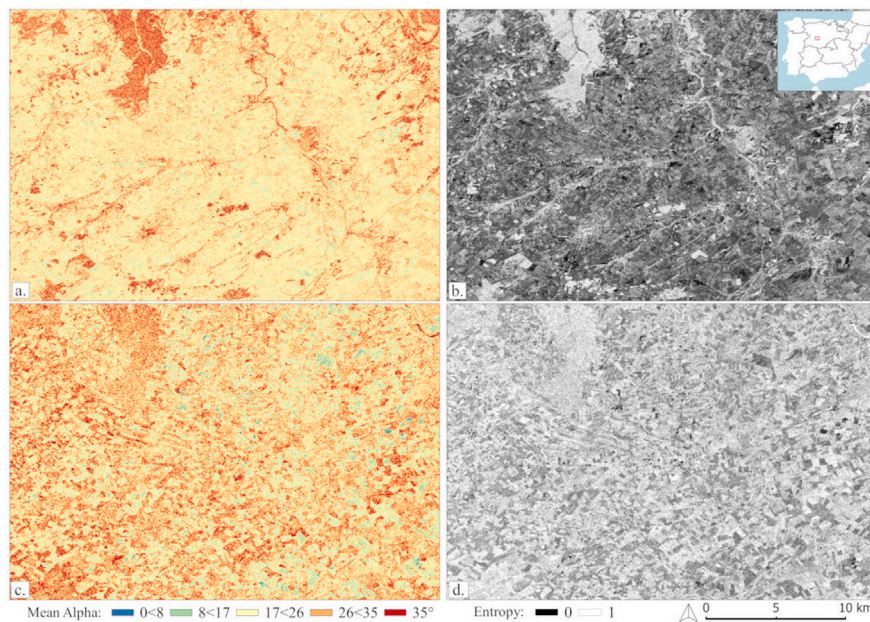
Fig. 6. Visual comparison between (a) SAOCOM $\bar{\alpha}$ image; (b) SAOCOM entropy image; (c) Sentinel-1 $\bar{\alpha}$ image; (d) Sentinel-1 entropy image. SAOCOM has been acquired at 2022-05-23, and Sentinel-1 at 2022-05-19.

2010). At the L-band the difference between the two polarization channels is larger than at the C-band, which is explicable by the fact that the VV backscattering contains more of the surface signal, whereas the VH is representative of volume backscattering (Mengen et al., 2021). On the other site, C-band, due to less penetration, contains signal contribution mainly from the canopy in both polarizations (Fig. 4) (Moran et al., 2011). Indeed, as NDVI increases, the difference between the two bands decreases, e.g. in Canizal, in summer, when the mean NDVI increases by 58%, the mean difference for VV and VH is about 2.1 dB lower for SAOCOM and 1.5 dB for Sentinel-1 in respect to the other seasons (Fig. 4). Stations where VV and VH absolute values are closer (e.g. LasTresRayas and Guarrati, with mean difference of 5.0 dB and 7.9 dB respectively), are characterized by an important scattering contribution from the canopy, contrary to stations where co- and cross-responses are well separated (e.g. ConcejodelMonte). This is confirmed by the expected sensitivity of the latter to soil moisture (R^2 of 0.61 for VV L-band, and 0.44 for VV C-band) whereas Guarrati and LasTresRayar show weak or no correlation (Fig. 7). LasTresRayar insensitivity to SSM is explained by its location in a tree/shrub-covered field, in which dihedral and volume components contribute significantly to the total backscatter. Co-cross polarization at C-band decreases from May to June for LasArenas, LasVacas, ConcejoddelMonte and CasaPeriles (Fig. 4), due to both a decrease in VV polarization and an increase in HV. This behavior is considered characteristic for wheat fields (Mattia et al., 1997; Balenzano et al., 2010) and has been interpreted in terms of backscatter attenuation during the elongation phase due to wheat vertical structure (Arias et al., 2022b). On the other side, SAOCOM amplitudes in cross-polarization have values below −15.7 dB (Section 3.1) as L-band signals interaction with small wheat dipole structures is limited. Indeed, in trees or shrub-cultivated fields, where larger structures such as branches are present, mean L-band VH values are 16.9% higher than the mean values registered in crop-cultivated fields. Some studies found that, especially for crops characterized by a vertical structure, the cross-polarizated channel at the C-band contains a significant soil backscattering signal, also less sensitive to other soil parameters (Moran et al., 2011; Balenzano et al., 2012). However, at the C-band, in any validation site, VH is not correlated to SSM, whereas at the L-band 5 stations show a slight positive R^2, comprised between 0.12 to 0.48 (Fig. 7), observed also by Anconitano et al. (2022). R^2 is 14% higher in copolarized data for Sentinel-1 and 17% for SAOCOM data, with

values up to about 0.75. The increased sensitivity of the co-polarized band with respect to the cross-pol, causes VV and VH regression lines to diverge with increasing SSM values over some stations, especially in SAOCOM acquisitions (Fig. 7). Correlation values decline (Section 3.2) in tree/shrub fields is stronger at cross-polarization.

4.2. Scattering mechanisms interpretation

The temporal variability of C and L-band backscatter γ^0 is affected by vegetation phenological stages, described as NDVI variations, and precipitation events, linked to soil and vegetation water content. NDVI is relatively low in each validation site: in winter higher values are found in Guarrati (0.26), in spring Guarrati (0.35), in summer in Canizal (0.25), and in autumn in Guarrati (0.12) station (Fig. 4); both these stations are located in irrigated fields. Regarding the precipitation, in 2022 the cumulative precipitation value is 367.1 mm, in line with the average for the period 1991–2020 (Météo climat, 2023). In Canizal, LasArenas, LasTresRayas, and Carretoro the amplitude values follow the NDVI trend but, when the precipitation increase in autumn, γ^0 increases even if NDVI declines. On average, for the precipitation of 09–15 December (44.7 m), γ^0 of Sentinel-1 increases −5 dB for VH and 0.4 dB for VV. In ConcejoDelMonte, LasArenas, Guarrati, and Granja-g stations γ^0 temporal profiles follow the increase in precipitation events in autumn and winter. As shown in Fig. 6, polarimetric parameters at L-band are more shaved and spatially stable, whereas at the C-band vegetation variability is more visible. This observation is in line with classification results obtained by Skriver (2011) and Ma et al. (2021), reporting better performances for crop discrimination using polarimetric parameters at C-band rather than at L-band. As shown in Fig. 5, for trees/shrub cover, the difference between entropy and $\bar{\alpha}$ values are less pronounced than in crop fields, where L-band is capable of detecting soil properties.

4.3. C- and L-band sensitivity to soil moisture

Overall, C- and L-bands follow comparable trends, with mean differences comprised between 1.4 dB (LasBodegas) and 7.4 dB (LasEritas) (Fig. 4). Sentinel-1 backscatter is stronger than SAOCOM, for a maximum difference of 18.1 dB. An exception is the LasTresRayas and LasBodegas stations, where the L-band response gets stronger than the
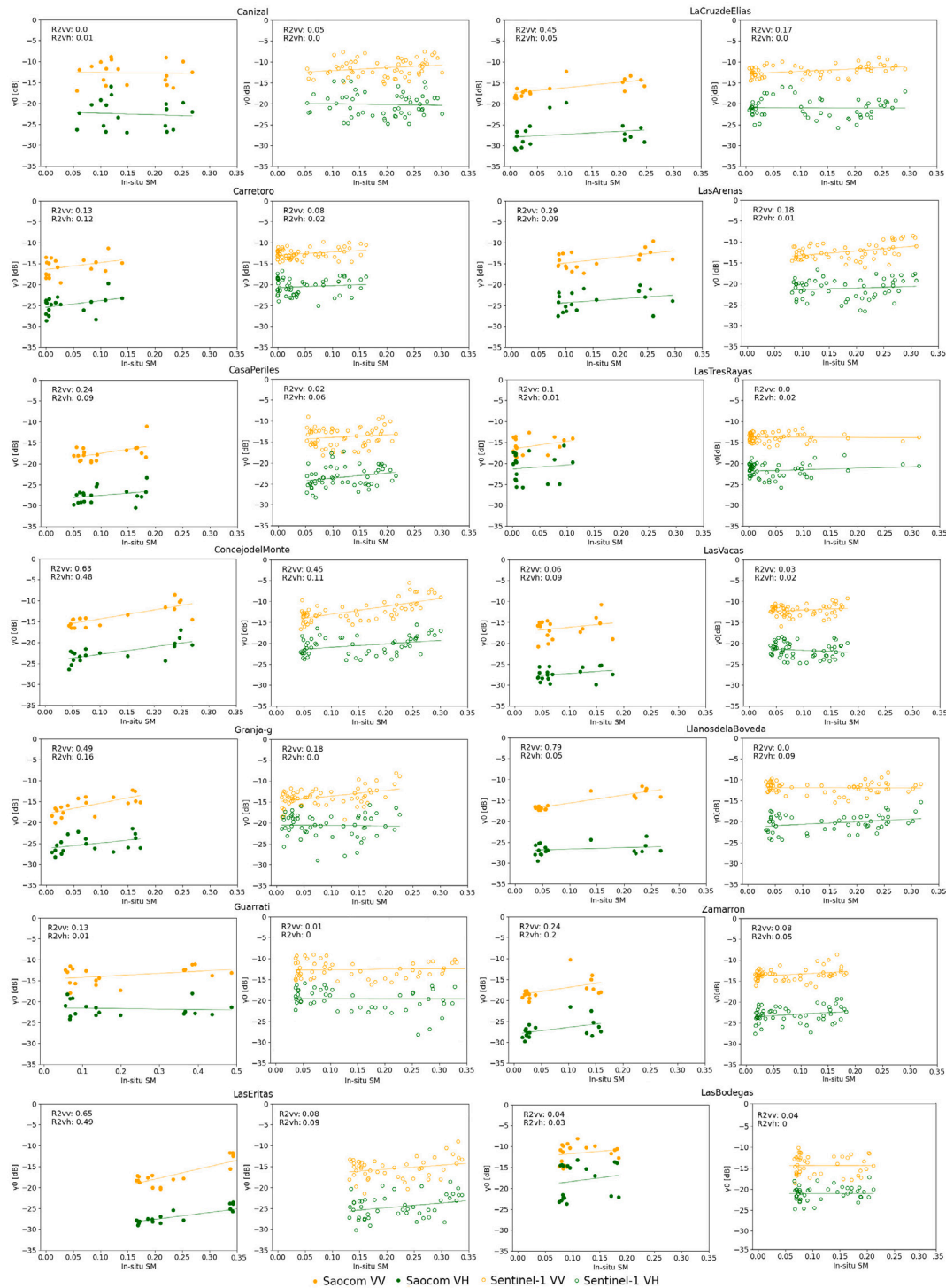
Fig. 7. Scatter plots of in-situ SSM and mean γ^0 values, over a viewing window of 9 samples, in each station considered. The coefficient of determination R^2 is reported for each band and polarization channel.

C-band from March to Jun. As CD estimates (Fig. 9) show a greater bias for the L-band in the same period, this increase does not reflect an increase in the dielectric constant but could be rather related to geometrical effects linked to the canopy development, which cause an increase in double-bounce effects (Li et al., 2019). Also, stations such as Carretoro and LasArenas, show the opposite behavior, with the VV backscattering at L-band decreasing from March to May by 23.0% and 44.5%, while VV at the C-band remains stable and VH at both

frequencies increases (as well as NDVI), and showing more correlation with SSM (Fig. 7). As expected, the scatterplots show a significantly higher correlation between γ^0 and in-situ SSM for the L-band than for the C-band (56% for the VV polarization), and in accordance to what found by Anconitano et al. (2022), where the correlation of SAOCOM and Sentinel-1 sigma-naught at VV polarization is respectively up to 0.51 and 0.25. Even if, in Fig. 7, R^2 are lower than expected, especially for C-band data, the change detection method retrievals reproduce
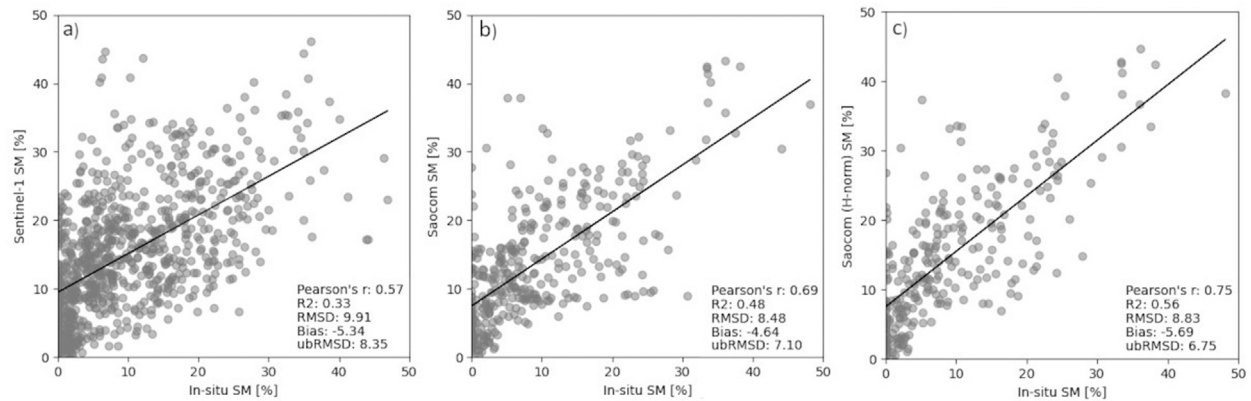
Fig. 8. Scatterplots between in situ and retrieved SSM for (a) C-band, (b) L-band not normalized, and (c) L-band normalized data.

the in-situ soil moisture trends (Fig. 9). Nevertheless, an evident bias characterizes the dry period estimates, from June to September, especially in Carretoro, LasVacas, Guarrati, and LasEritas: retrieved soil moisture values are consistently higher than the in situ measurements. This behavior has been observed for SMAP data and was attributed to dry subsurface (Wagner et al., 2013) (Section 2.1.1). The L band shows an improvement limited to LlandosdeLaBoveda and LaCruzdeElias, and canopy interactions complicate the interpretation. The scatterplots between the measured and retrieved soil moisture revealed that L-band data obtain retrieval accuracy expressed with RMSD, ubRMSD, and R^2 of 14.4%, 14.9% and 31.6% higher than C-band data (Fig. 8). Fig. 9 shows that at both frequencies, the model is more accurate in autumn and winter (17%) than in summer and spring when SSM is overestimated. This behavior is more pronounced at the C-band (21%), and can be justified by vegetation changes, harvesting, and plowing activities γ^0. The normalized procedure causes the bias to increase, indicating a shift from the soil moisture retrieved and measured; nevertheless, the relative trend, expressed by the R^2 and the ubRMSE, improves. Better performances for L-band data, despite the lesser temporal frequency (Fig. 2), differ from other findings (Cui et al., 2022; El Hajj et al., 2019; Sekertekin et al., 2020; Hosseini and McNairn, 2017) in which L-band (ALOS-2) obtained higher RMSE in respect to Sentinel-1. However, these comparisons are biased by either the use, for the L-band, of HH channels, which enhances double bounce, or UAVSAR data with differences in temporal coverage. Whereas, Balenzano et al. (2010), by applying a CD model and HH channels obtained a better accuracy for L band compared to C-band in every crop type. This also points out that the potential improvement of longer wavelength depends, other than on the land cover type (Zribi et al., 2019), by the model considered, and it is maximized in CD approaches, which do not explicitly model the vegetation's contribution.

5. Conclusions

This work compared SAOCOM L-band and Sentinel-1 C-band data for SSM retrieval underneath sparse and agricultural fields over a semi-arid region in Spain. Moreover, a novel roughness normalization procedure for SAOCOM data based on the entropy parameter was proposed. The main results and implications are summarized below:

1. L-band γ^0_{VV} is the best configuration for SSM retrieval, with a positive correlation observed in 3/4 of the validation sites. Temporal series of C-band γ^0 have shown response to NDVI variation but low correlation with in-situ SSM.
2. Co- and cross-polarization difference analysis, as well as $\bar{\alpha}$ and entropy, demonstrated to provide information on the type of scattering mechanism at both frequencies, which help the interpretation of different sensitivity to SSM.

3. Change detection models obtained an ubRMSD of 0.071 m³/m³ for L-band data and 0.083 m³/m³ for C-band data, with a retrieval 14.3% more accurate for SAOCOM then for Sentinel-1 data. In the regressions, SAOCOM data obtained a R^2 value 22.9% higher with respect to Sentinel-1, whereas in the model SAOCOM outperformed by 14.9%.
4. The application of the proposed roughness normalization procedure led to an ubRMSD of 6.7% for SAOCOM, improving the retrieved soil moisture trend of 7.9%. Nevertheless, the increase in trend accuracy, indicated by an increase in R^2 and $ubRMSD$ values, corresponds to a decrease in absolute SSM values accuracy, thus a larger bias.

The better performance of L-band data, despite lower temporal frequency, is a promising result in the view of the forthcoming NISAR and Rose-L SAR satellites. The CD algorithm, applied at different frequencies with no changes, shows good versatility. The retrieval biases, noticed from April to September for both the frequencies, points out the need to consider vegetation and roughness effect, especially when data are used at high resolutions. A roughness normalization procedure was proposed; however, as entropy is also sensitive to the canopy structure, the feasibility of this procedure depends on the presence of vegetation. Therefore, reliable knowledge of crop phases, irrigation practices, and agricultural work is crucial for assessing the sensitivity of C- and L-band to soil moisture over various cultivation types, and constitutes a limit for this analysis. In addition, this study relies on the use of terrain flattened γ^0 to normalize the backscatter from the influence of the acquisition's geometry. However, orbit-dependent small-scale effects, linked to the orientations of individual features in the fields, may bias this comparison. Finally, the use of a longer and more detailed temporal series, in terms of temporal frequency and variability in the ground conditions, would have increased the generalizability of the results, necessary to guide methodological strategy to the integration of multifrequency bands. Issues related to different acquisition geometries, inhomogeneity of temporal coverage, and frequency-dependent non-linear backscatter mechanisms require further study in order to achieve the interoperability of C-band and L-band, and thus the expected improvements in terms of the possibility to operate over a wider range of vegetation cover and temporal resolution.

CRediT authorship contribution statement

Benedetta Brunelli: Writing – original draft, Methodology, Investigation, Formal analysis, Conceptualization. **Francesco Mancini:** Writing – review & editing, Supervision, Investigation, Conceptualization.
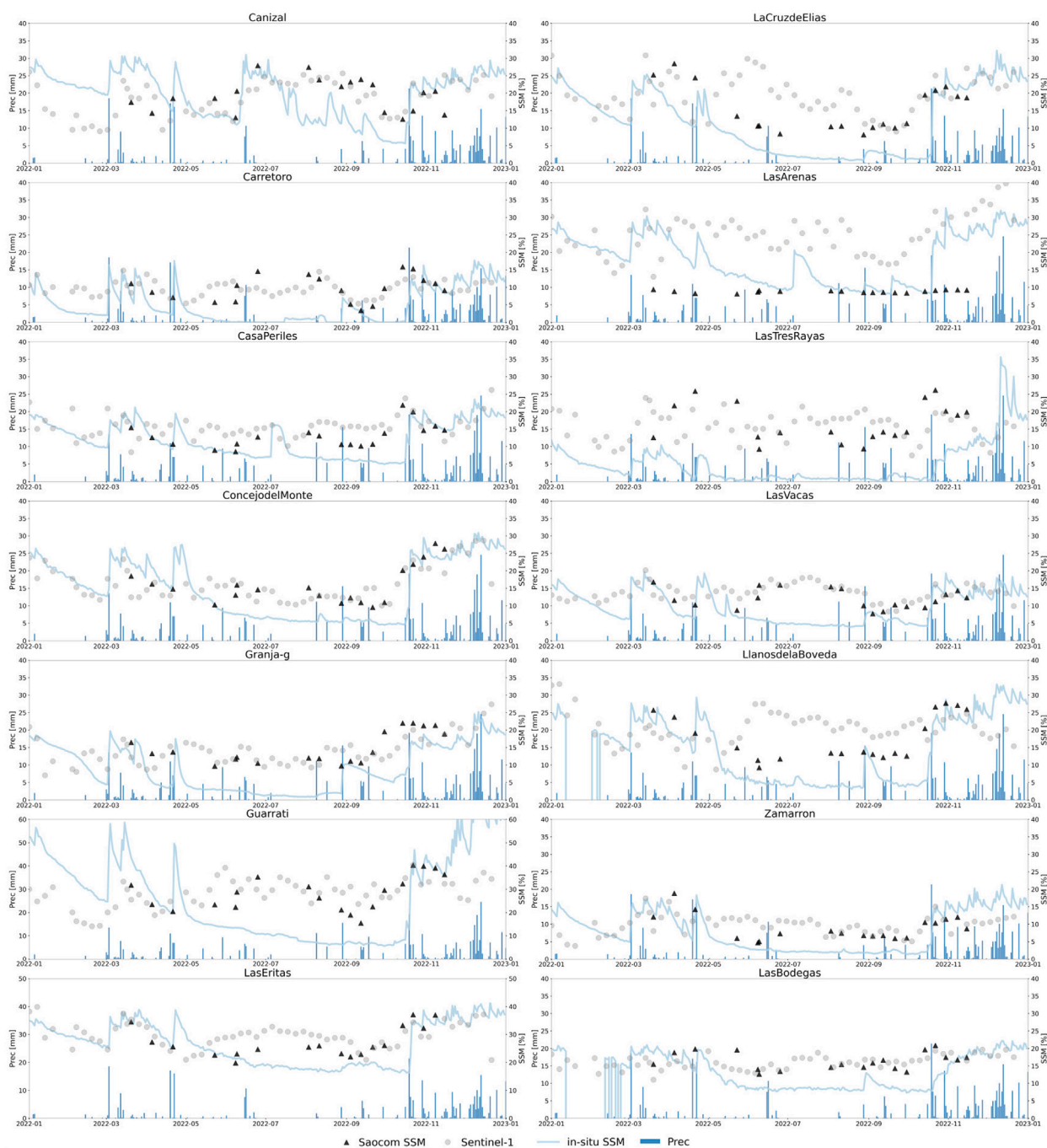
Fig. 9. Comparison of the retrievals obtained with C- and L-band (not normalized data). Triangles indicate SAOCOM acquisitions and points Sentinel-1.

Declaration of competing interest

The authors declare that they have no known competing financial interests or personal relationships that could have appeared to influence the work reported in this paper.

Data availability

The authors do not have permission to share data.

References

Abdikan, S., Sekertekin, A., Madenoglu, S., Ozcan, H., Peker, M., Pinar, M.O., Koc, A., Akgul, S., Secmen, H., Kececi, M., et al., 2023. Surface soil moisture estimation from multi-frequency SAR images using ANN and experimental data on a semi-arid environment region in Konya, Turkey. Soil Tillage Res. 228, 105646.

Alonso-Gonzalez, A., Papathanassiou, K.P., 2022. Multi-frequency polarimetric change analysis for agricultural monitoring. In: EUSAR 2022; 14th European Conference on Synthetic Aperture Radar. VDE, pp. 1–6.

Anconitano, G., Acuña, M.A., Guerriero, L., Pierdicca, N., 2022. Analysis of multi-frequency SAR data for evaluating their sensitivity to soil moisture over an agricultural area in Argentina. In: IGARSS 2022-2022 IEEE International Geoscience and Remote Sensing Symposium. IEEE, pp. 5716–5719.

Arias, M., Campo-Bescós, M.Á., Álvarez-Mozos, J., 2022a. On the influence of acquisition geometry in backscatter time series over wheat. Int. J. Appl. Earth Obs. Geoinf. 106, 102671.

Arias, M., Campo-Bescós, M.Á., Arregui, L.M., González-Audícana, M., Álvarez-Mozos, J., 2022b. A new methodology for wheat attenuation correction at C-band VV-polarized backscatter time series. IEEE Trans. Geosci. Remote Sens. 60, 1–14.

Azcueta, M., Gonzalez, J.P.C., Zajc, T., Ferreyra, J., Thibeault, M., 2021. External calibration results of the SAOCOM-1A commissioning phase. IEEE Trans. Geosci. Remote Sens. 60, 1–8.

Baghdadi, N., Dubois-Fernandez, P., Dupuis, X., Zribi, M., 2012. Sensitivity of main polarimetric parameters of multifrequency polarimetric SAR data to soil moisture and surface roughness over bare agricultural soils. IEEE Geosci. Remote Sens. Lett. 10 (4), 731–735.

Balenzano, A., Mattia, F., Satalino, G., Davidson, M.W., 2010. Dense temporal series of C-and L-band SAR data for soil moisture retrieval over agricultural crops. IEEE J. Sel. Top. Appl. Earth Obs. Remote Sens. 4 (2), 439–450.

Balenzano, A., Mattia, F., Satalino, G., Ouellette, J., Johnson, J.T., 2012. An experimental and theoretical study on the sensitivity of cross-polarized backscatter to soil moisture. In: 2012 IEEE International Geoscience and Remote Sensing Symposium. IEEE, pp. 3411–3414.

Banque, X., Lopez-Sanchez, J.M., Monells, D., Ballester, D., Duro, J., Koudogbo, F., 2015. Polarimetry-based land cover classification with sentinel-1 data. POLINSAR 2015 729, 13.

Bauer-Marschallinger, B., Freeman, V., Cao, S., Paulik, C., Schaufler, S., Stachl, T., Modanesi, S., Massari, C., Ciabatta, L., Brocca, L., et al., 2018. Toward global soil moisture monitoring with sentinel-1: Harnessing assets and overcoming obstacles. IEEE Trans. Geosci. Remote Sens. 57 (1), 520–539.

Bhogapurapu, N., Dey, S., Mandal, D., Bhattacharya, A., Karthikeyan, L., McNairn, H., Rao, Y., 2022. Soil moisture retrieval over croplands using dual-pol L-band GRD SAR data. Remote Sens. Environ. 271, 112900. http://dx.doi.org/10.1016/j.rse.2022.112900.

Brunelli, B., De Giglio, M., Magnani, E., Dubbini, M., 2023. Surface soil moisture estimate from sentinel-1 and sentinel-2 data in agricultural fields in areas of high vulnerability to climate variations: the marche region (Italy) case study. Environ. Dev. Sustain. 1–23.

Cloude, S.R., Pottier, E., 1996. A review of target decomposition theorems in radar polarimetry. IEEE Trans. Geosci. Remote Sens. 34 (2), 498–518.

Cui, H., Jiang, L., Paloscia, S., Santi, E., Pettinato, S., Wang, J., Fang, X., Liao, W., 2022. The potential of ALOS-2 and sentinel-1 radar data for soil moisture retrieval with high spatial resolution Over Agroforestry Areas, China. IEEE Trans. Geosci. Remote. Sens. 60, 1–17.

Dorigo, W., Himmelbauer, I., Aberer, D., Schremmer, L., Petrakovic, I., Zappa, L., Preimesberger, W., Xaver, A., Annor, F., Ardö, J., et al., 2021. The international soil moisture network: serving earth system science for over a decade. Hydrol. Earth Syst. Sci. 25 (11), 5749–5804.

Dostalova, A., Navacchi, C., Greimeister-Pfeil, I., Small, D., Wagner, W., 2022. The effects of radiometric terrain flattening on SAR-based forest mapping and classification. Remote Sens. Lett. 13 (9), 855–864.

El Hajj, M., Baghdadi, N., Zribi, M., 2019. Comparative analysis of the accuracy of surface soil moisture estimation from the C- and L-bands. Int. J. Appl. Earth Obs. Geoinf. 82, 101888. http://dx.doi.org/10.1016/j.jag.2019.05.021.

Entekhabi, D., Reichle, R.H., Koster, R.D., Crow, W.T., 2010. Performance metrics for soil moisture retrievals and application requirements. J. Hydrometeorol. 11 (3), 832–840.

Fung, A.K., Li, Z., Chen, K.-S., 1992. Backscattering from a randomly rough dielectric surface. IEEE Trans. Geosci. Remote Sens. 30 (2), 356–369.

Graldi, G., Vitti, A., 2022. Identifying time patterns at the field scale for retrieving superficial soil moisture on AN agricultural area with a change detection method: a preliminary analysis. Int. Arch. Photogramm. Remote Sens. Spatial Inf. Sci. 43, 879–886.

Gururaj, P., Umesh, P., Shetty, A., 2021. Assessment of surface soil moisture from ALOS PALSAR-2 in small-scale maize fields using polarimetric decomposition technique. Acta Geophys. 69, 579–588.

Hajnsek, I., Pottier, E., Cloude, S.R., 2003. Inversion of surface parameters from polarimetric SAR. IEEE Trans. Geosci. Remote Sens. 41 (4), 727–744.

Hamze, M., Baghdadi, N., El Hajj, M.M., Zribi, M., Bazzi, H., Cheviron, B., Faour, G., 2021. Integration of L-band derived soil roughness into a bare soil moisture retrieval approach from C-band SAR data. Remote Sens. 13 (11), 2102.

Harfenmeister, K., Itzerott, S., Weltzien, C., Spengler, D., 2021. Agricultural monitoring using polarimetric decomposition parameters of sentinel-1 data. Remote Sens. 13 (4), 575.

Hosseini, M., McNairn, H., 2017. Using multi-polarization C-and L-band synthetic aperture radar to estimate biomass and soil moisture of wheat fields. Int. J. Appl. Earth Obs. Geoinf. 58, 50–64.

Ji, K., Wu, Y., 2015. Scattering mechanism extraction by a modified cloude-pottier decomposition for dual polarization SAR. Remote Sens. 7 (6), 7447–7470.

Kim, Y., Van Zyl, J.J., 2009. A time-series approach to estimate soil moisture using polarimetric radar data. IEEE Trans. Geosci. Remote Sens. 47 (8), 2519–2527.

Koch, M., Schmid, T., Reyes, M., Gumuzzio, J., 2012. Evaluating full polarimetric C-and L-band data for mapping wetland conditions in a semi-arid environment in central Spain. IEEE J. Sel. Top. Appl. Earth Obs. Remote Sens. 5 (3), 1033–1044.

Li, J., Xia, E., Wang, L., Yan, K., Zhu, L., Huang, J., 2022. Knowledge domain and emerging trends of climate-smart agriculture: A bibliometric study. Environ. Sci. Pollut. Res. 29 (46), 70360–70379.

Li, H., Zhang, C., Zhang, S., Atkinson, P.M., 2019. Full year crop monitoring and separability assessment with fully-polarimetric L-band UAVSAR: A case study in the sacramento valley, california. Int. J. Appl. Earth Obs. Geoinf. 74, 45–56.

Liu, P.-W., Judge, J., DeRoo, R.D., England, A.W., Bongiovanni, T., Luke, A., 2016. Dominant backscattering mechanisms at L-band during dynamic soil moisture conditions for sandy soils. Remote Sens. Environ. 178, 104–112.

Ma, T., Han, L., Liu, Q., 2021. Retrieving the soil moisture in bare farmland areas using a modified Dubois model. Front. Earth Sci. 1216.

Magagi, R., Jammali, S., Goïta, K., Wang, H., Colliander, A., 2022. Potential of L-and C-bands polarimetric SAR data for monitoring soil moisture over forested sites. Remote Sens. 14 (21), 5317.

Mattia, F., Le Toan, T., Souyris, J.-C., De Carolis, C., Floury, N., Posa, F., Pasquariello, N., 1997. The effect of surface roughness on multifrequency polarimetric sar data. IEEE Transac. Geosci. Remote Sens. 35 (4), 954–966.

Mengen, D., Montzka, C., Jagdhuber, T., Fluhrer, A., Brogi, C., Baum, S., Schüttemeyer, D., Bayat, B., Bogena, H., Coccia, A., et al., 2021. Sarsense: Analyzing air-and space-borne C-and L-band SAR backscattering signals to changes in soil and plant parameters of crops. In: 2021 IEEE International Geoscience and Remote Sensing Symposium IGARSS. IEEE, pp. 6092–6095.

Météo climat, 2023. Météo climat stats Moyennes 1991/2020 Espagne. http://meteo-climat-bzh.dyndns.org/listenormale-1991-2020-3-p62.php. (Accessed: 2023-06-28).

Moran, M.S., Alonso, L., Moreno, J.F., Mateo, M.P.C., De La Cruz, D.F., Montoro, A., 2011. A RADARSAT-2 quad-polarized time series for monitoring crop and soil conditions in Barrax, Spain. IEEE Trans. Geosci. Remote Sens. 50 (4), 1057–1070.

Oh, Y., Sarabandi, K., Ulaby, F.T., 1992. An empirical model and an inversion technique for radar scattering from bare soil surfaces. IEEE Trans. Geosci. Remote Sens. 30 (2), 370–381.

Pablos, M., Martínez-Fernández, J., Piles, M., Sánchez, N., Vall-llossera, M., Camps, A., 2016. Multi-temporal evaluation of soil moisture and land surface temperature dynamics using in situ and satellite observations. Remote Sens. 8 (7), 587.

Petropoulos, G.P., Ireland, G., Barrett, B., 2015. Surface soil moisture retrievals from remote sensing: Current status, products & future trends. Phys. Chem. Earth, Parts A/B/C 83, 36–56.

Preimesberger, W., Stradiotti, P., Scherrer, S.A., Tercjak, M., Bakcsa, Z., Boresch, A., Dorigo, W.A., Aberer, D., Himmelbauer, I., GIBON, F., et al., 2022. QA4SM-An online validation service for EO soil moisture data users and producers.

Recchia, A., Giudici, D., Albinet, C., 2022. SAOCOM 1A/B quality assessment summary. EDAO, Telespazio. Issue 2.0.

Rosenqvist, A., Frulla, L., Milovich, M., Thibeault, M., Palomeque, M., Zajc, T., 2014. A brief overview of the SAOCOM integrated mission acquisition strategy (IMAS). In: Proceedings of the 1st ESA SAOCOM Companion Satellite Workshop, ESA ESTEC. pp. 0–35.

Sekertekin, A., Marangoz, A.M., Abdikan, S., 2020. ALOS-2 and sentinel-1 SAR data sensitivity analysis to surface soil moisture over bare and vegetated agricultural fields. Comput. Electron. Agric. 171, 105303.

Seppi, S.A., López-Martinez, C., Joseau, M.J., 2022. Assessment of L-Band SAOCOM InSAR coherence and its comparison with C-Band: A case study over managed forests in Argentina. Remote Sens. 14 (22), 5652.

Skriver, H., 2011. Crop classification by multitemporal C-and L-band single-and dual-polarization and fully polarimetric SAR. IEEE Trans. Geosci. Remote Sens. 50 (6), 2138–2149.

Small, D., 2011. Flattening Gamma: Radiometric terrain correction for SAR imagery. IEEE Trans. Geosci. Remote Sens. 49 (8), 3081–3093. http://dx.doi.org/10.1109/TGRS.2011.2120616.

Wagner, W., Brocca, L., Naeimi, V., Reichle, R., Draper, C., De Jeu, R., Ryu, D., Su, C.-H., Western, A., Calvet, J.-C., et al., 2013. Clarifications on the "Comparison between SMOS, VUA, ASCAT, and ECMWF soil moisture products over four watersheds in US". IEEE Trans. Geosci. Remote Sens. 52 (3), 1901–1906.

Wagner, W., Lemoine, G., Borgeaud, M., Rott, H., 1999a. A study of vegetation cover effects on ERS scatterometer data. IEEE Trans. Geosci. Remote Sens. 37 (2), 938–948.

Wagner, W., Lemoine, G., Rott, H., 1999b. A method for estimating soil moisture from ERS scatterometer and soil data. Remote Sens. Environ. 70 (2), 191–207.

Widhalm, B., Bartsch, A., Goler, R., 2018. Simplified normalization of C-band synthetic aperture radar data for terrestrial applications in high latitude environments. Remote Sens. 10 (4), 551.

Zribi, M., Muddu, S., Bousbih, S., Al Bitar, A., Tomer, S.K., Baghdadi, N., Bandyopadhyay, S., 2019. Analysis of L-band SAR data for soil moisture estimations over agricultural areas in the tropics. Remote Sens. 11 (9), 1122.